

Two-dimensional Sb net generated nontrivial topological states in $SmAgSb_2$ probed by quantum oscillations

Jian Yuan(袁健), Xian-Biao Shi(石贤彪), Hong Du(杜红), Tian Li(李田), Chuan-Ying Xi(郗传英), Xia Wang(王霞), Wei Xia(夏威), Bao-Tian Wang(王保田), Rui-Dan Zhong(钟瑞丹), and Yan-Feng Guo(郭艳峰)

Citation: Chin. Phys. B, 2024, 33 (**7**): 077102. DOI: 10.1088/1674-1056/ad4bc2
Journal homepage: http://cpb.iphy.ac.cn; http://iopscience.iop.org/cpb

What follows is a list of articles you may be interested in

Spin direction dependent quantum anomalous Hall effect in two-dimensional ferromagnetic materials

Yu-Xian Yang(杨宇贤) and Chang-Wen Zhang(张昌文)
Chin. Phys. B, 2024, 33 (**4**): 047101. DOI: 10.1088/1674-1056/ad1380

Design of sign-reversible Berry phase effect in 2D magneto-valley material

Yue-Tong Han(韩曰通), Yu-Xian Yang(杨宇贤), Ping Li(李萍), and Chang-Wen Zhang(张昌文)
Chin. Phys. B, 2023, 32 (**9**): 097101. DOI: 10.1088/1674-1056/acd920

Intrinsic V vacancy and large magnetoresistance in $V_{1-\delta}Sb_2$ single crystal

Yong Zhang(张勇), Xinliang Huang(黄新亮), Jinglei Zhang(张警蕾), Wenshuai Gao(高文帅), Xiangde Zhu(朱相德), and Li Pi(皮雳)
Chin. Phys. B, 2022, 31 (**3**): 037102. DOI: 10.1088/1674-1056/ac3070

Negative differential resistance and quantum oscillations in $FeSb_2$ with embedded antimony

Fangdong Tang(汤方栋), Qianheng Du(杜乾衡), Cedomir Petrovic, Wei Zhang(张威), Mingquan He(何明全), Liyuan Zhang(张立源)
Chin. Phys. B, 2019, 28 (**3**): 037104. DOI: 10.1088/1674-1056/28/3/037104

Quantum oscillation measurements in high magnetic field and ultra-low temperature

Pu Wang(王瀑), Gang Li(李岗), Jian-Lin Luo(雒建林)
Chin. Phys. B, 2018, 27 (**7**): 077101. DOI: 10.1088/1674-1056/27/7/077101

RAPID COMMUNICATION

Two-dimensional Sb net generated nontrivial topological states in $SmAgSb_2$ probed by quantum oscillations

Jian Yuan(袁健)[1], Xian-Biao Shi(石贤彪)[2,†], Hong Du(杜红)[3], Tian Li(李田)[4], Chuan-Ying Xi(郗传英)[5], Xia Wang(王霞)[1], Wei Xia(夏威)[1,6,‡], Bao-Tian Wang(王保田)[2], Rui-Dan Zhong(钟瑞丹)[3,§], and Yan-Feng Guo(郭艳峰)[1,6]

[1] *School of Physical Science and Technology, ShanghaiTech University, Shanghai* 201210, *China*
[2] *Institute of High Energy Physics, Chinese Academy of Sciences, Beijing* 100049, *China*
[3] *Tsung-Dao Lee Institute, Shanghai Jiao Tong University, Shanghai* 200240, *China*
[4] *Xingzhi College, Zhejiang Normal University, Jinhua* 321100, *China*
[5] *Anhui Province Key Laboratory of Condensed Matter Physics at Extreme Conditions, High Magnetic Field Laboratory of the Chinese Academy of Sciences, Hefei* 230031, *China*
[6] *ShanghaiTech Laboratory for Topological Physics, ShanghaiTech University, Shanghai* 201210, *China*

(Received 8 May 2024; revised manuscript received 13 May 2024; accepted manuscript online 15 May 2024)

The REAgSb$_2$ (RE = rare earth and Y) family has drawn considerable research interest because the two-dimensional Sb net in their crystal structures hosts topological fermions and hence rich topological properties. We report herein the magnetization and magnetotransport measurements of $SmAgSb_2$ single crystal, which unveil very large magnetoresistance and high carrier mobility up to 6.2×10^3% and 5.58×10^3 cm^2·V^{-1}·s^{-1}, respectively. The analysis of both Shubnikov–de Haas and de Haas–van Alphen quantum oscillations indicates nontrivial Berry phases in the paramagnetic state while trivial Berry curvature in the antiferromagnetic state, indicating a topological phase transition induced by the antiferromagnetic order. It is also supported by the first-principles calculations. The results not only provide a new interesting topological material but also offer valuable insights into the correlation between magnetism and nontrivial topological states.

Keywords: large magnetoresistance, quantum oscillations, topological phase transition

PACS: 71.20.Eh, 75.47.–m, 75.50.Ee **DOI:** 10.1088/1674-1056/ad4bc2

1. Introduction

The topological phases, such as Dirac and Weyl semimetals, have captured a surge of interest due to that they host relativistic Dirac or Weyl fermions which can produce rich topological physics.[1–11] Among them, the magnetic topological phases are especially attractive because the interplay between magnetism and nontrivial topological states can serve as a source for unconventional bulk transport properties, anomalous surface or edge states, such as the quantum anomalous Hall effect, unconventional superconductivity, magnetopiezoelectric effect, anomalous Hall effect (AHE), anomalous Nernst effect, etc.[12–32] The 112-type layered compounds $LnTPn_2$ (Ln = Ca–Ba, Eu, Yb; T = Mn, Zn; Pn = Sb, Bi) have a large family of topological phases that offer opportunities to probe the correlation between magnetism and nontrivial topological states. Both experimental and theoretical investigations on AMnBi$_2$ (A = Sr, Ba) and AMnSb$_2$, which host two-dimensional (2D) Bi/Sb layer, unveil Dirac or Weyl fermions near the Fermi level (E_F).[19–23] The angle-resolved photoemission spectroscopy measurements on La/CeAgSb$_2$ reveal a Dirac band in the 2D Sb layer.[33,34] The study of YbMnBi$_2$ indicates that Mn atoms contribute weak magnetism that can break the time reversal symmetry, resulting in the Weyl states.[30] To achieve a comprehension of the intriguing topological properties of $LnTPn_2$, more studies are very necessary, which would also be very valuable to yield fruitful insights into the long-standing issue in magnetic topological physics.

In this work, we have investigated the nontrivial topological states in $SmAgSb_2$ crystals via measuring the magnetizations and magnetotransport properties, also with the assistance of first-principles calculations. The results unveil large magnetoresistance and high carrier mobility in this material. The analysis of the de Haas–van Alphen (dHvA) and Shubnikov–de Haas (SdH) quantum oscillations also exposes a topological phase transition tightly related to the antiferromagnetic (AFM) order in $SmAgSb_2$.

2. Experimental details

Single crystals of $SmAgSb_2$ were grown by using the self-flux method. High purity elements of Sm lumps (99.9%), Ag powders (99.9%) and antimony lumps (99.999%) were mixed

†Corresponding author. E-mail: shixb@ihep.ac.cn
‡Corresponding author. E-mail: xiawei2@shanghaitech.edu.cn
§Corresponding author. E-mail: rzhong@sjtu.edu.cn

© 2024 Chinese Physical Society and IOP Publishing Ltd

in a molar ratio of 1:1:20 placed into an alumina crucible which was then sealed into a quartz tube in vacuum. The assembly was heated in a furnace up to 1100 °C within 20 hours, kept at that temperature for 20 hours, and then slowly cooled down to 700 °C within 200 hours. The excess antimony flux was removed at this temperature by quickly placing the assembly into a high-speed centrifuge.

The crystallographic phase and quality of $SmAgSb_2$ were examined on the Bruker D8 advance powder x-ray diffractometer (PXRD) with Cu $K\alpha_1$ ($\lambda = 1.5408$ Å) at 298 K and also on the Bruker D8 single crystal x-ray diffractometer with Mo $K\alpha_1$ ($\lambda = 0.71073$ Å). The single crystal x-ray diffraction (SXRD) data was analyzed by using the software APEX3. Magnetization measurements on the $SmAgSb_2$ crystals were performed in a commercial Quantum Design 7 T magnetic properties measurement system (MPMS). The electrical and magneto-transport measurements were performed in a commercial Quantum Design 9 T DynaCool physical properties measurement system (PPMS). The magnetotransport was also measured in the Steady High Magnetic Field Facility at Hefei (SHMFF).

The first-principles calculations were carried out within the framework of the projector augmented wave (PAW) method,[35,36] and employed the generalized gradient approximation (GGA) with Perdew–Burke–Ernzerhof (PBE) formula,[37,38] as implemented in the Vienna *ab initio* simulation package (VASP).[39–41] For all calculations, the cutoff energy for the plane-wave basis was set to 500 eV, the Brillouin zone (BZ) sampling was done with a Γ-centered Monkhorst–Pack k-point mesh of size $20 \times 20 \times 8$, and the total energy difference criterion was defined as 10^{-6} eV for self-consistent convergence. The GGA + U ($U = 6$ eV)[42] scheme was utilized to consider the effect of Coulomb repulsion in the Sm-4f orbital. The Wannier90 package[43] was adopted to construct Wannier functions from the first-principles results. The WannierTools code[44] was used to investigate the topological features for both paramagnetic (PM) and AFM states.

3. Results

Our analysis of the SXRD data achieves the best solutions supporting the centrosymmetric space group of *P*4/*nmm* with lattice parameters $a = b = 4.3174(6)$ Å, $c = 10.5573(17)$ Å, $\alpha = \beta = \gamma = 90°$. On this basis, the schematic crystal structure is presented in Figs. 1(a) and 1(b), which is featured by the stacked ···–Sb–Sm–[Sb–Ag–Sb]–Sm–··· layers along the c axis and the 2D square net formed by the Sb layer. The temperature (T) dependence of longitudinal resistivity ρ measured with electrical current I along the (001) plane under a magnetic field $B = 0$ T is presented in the Fig. 1(c), showing a typical semimetallic behavior. A clear kink signifying the AFM order is also visible at around 9 K seen in the lower right inset, consistent with the result of magnetic susceptibilities $\chi(T)$ as shown in the upper left inset of Fig. 1(c).[45–47] The residual resistance ratio (*RRR*) [$\rho(300\ \mathrm{K})/\rho(3\ \mathrm{K})$] is about 146, implying the high quality of the single crystal. Figure 1(d) shows the room temperature PXRD of $SmAgSb_2$. The index on the clean diffraction peaks arising from the (001) surface of the crystal is consistent with the crystal structure obtained from SXRD analysis, which guarantees the correct phase and high quality of the crystals used in this study. The temperature- and magnetic field-dependent longitudinal resistivity ρ_{xx} is summarized in Fig. 2(a) with the magnetic field B along the [001] direction in the range of $[-9, 9]$ T. The $\rho_{xx}(B)$ within the temperature range of 3 K–15 K exhibits a quadratic-like behavior when B is large. Moreover, SdH quantum oscillations are observed in Figs. 2(a) and 2(b) in both $\rho_{xx}(B)$ and the Hall resistivity $\rho_{xy}(B)$, as shown in Fig. 2(b). The $\rho_{xy}(B)$ displays a nonlinear dependence on B with a negative slope, indicating that multiple types of carriers dominate the transport. To quantitatively estimate the densities and mobilities of these carriers in $SmAgSb_2$, the Hall resistivity is fitted by using a two-band model[48–50]

$$\rho_{xy} = \frac{B}{e}\frac{\left(n_{\mathrm{h}}\mu_{\mathrm{h}}^2 - n_{\mathrm{e}}\mu_{\mathrm{e}}^2\right) + \left(n_{\mathrm{h}} - n_{\mathrm{e}}\right)\mu_{\mathrm{e}}^2\mu_{\mathrm{h}}^2 B^2}{\left(n_{\mathrm{h}}\mu_{\mathrm{h}} + n_{\mathrm{e}}\mu_{\mathrm{e}}\right)^2 + \left(n_{\mathrm{h}} - n_{\mathrm{e}}\right)^2\mu_{\mathrm{e}}^2\mu_{\mathrm{h}}^2 B^2},$$

where n_{e} (n_{h}) denotes the carrier density of electron (hole), and $\mu_{\mathrm{e}}(\mu_{\mathrm{h}})$ is the mobility of the electron (hole). The insets of Fig. 2(b) show the perfect fitting at 3 K and 15 K, which at 3 K gives the carriers densities n_{e} of 6.46×10^{21} cm^{-3} and n_{h} of 0.8×10^{19} cm^{-3} and the corresponding mobilities of 159.57 cm^2·V^{-1}·s^{-1} and 5.58×10^3 cm^2·V^{-1}·s^{-1}, respectively. The fitting results of temperature-dependent densities and mobilities for both electron and hole carriers are summarized in Figs. 2(c) and 2(d), respectively. It is clear that the electron density is nearly three orders of magnitude larger than that of hole, while the mobility of the hole is far greater than that of the electron. Since $\rho_{xy}(B)$ exhibits linearity at $B > 2$ T, it seems that the deviation is caused by AHE originated from nontrivial Berry phase. However, the two-band model fits the data perfectly without the aid of any constant parameters to account for the AHE at both 3 K and 15 K. This strongly indicates that the deviation is due to the presence of multiple types of carriers. On the other hand, the calculated band structures, as reported previously,[45] show that the Fermi level crosses more conduction bands, which is consistent with the experimental findings. The hole density n_{h} increases as the temperature increases to 8 K and drops dramatically at 9 K. Conversely, the electron density n_{e} and the mobilities μ_{e} and μ_{h} decrease until they reach a temperature of 9 K which coincides with the AFM transition.

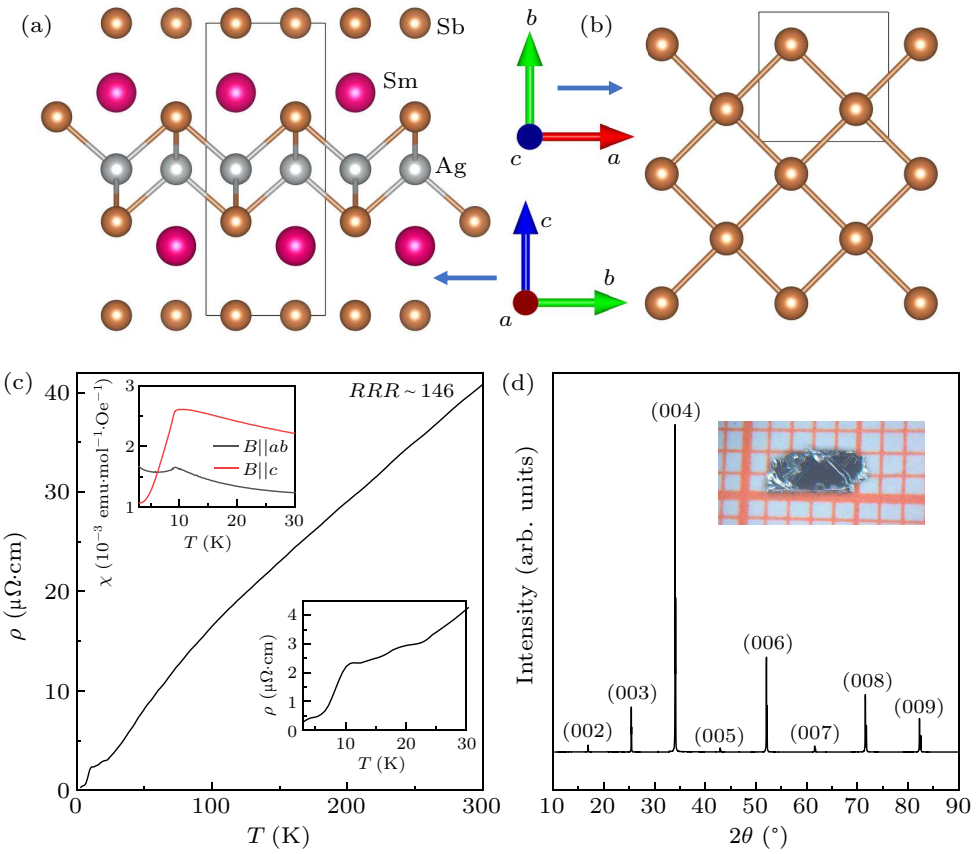


Fig. 1. Crystal structures of $SmAgSb_2$ viewed along the (a) [100] and (b) [001] directions. (c) The temperature-dependent electrical resistivity. The upper left inset plots the temperature-dependent magnetic susceptibilities with $B\|ab$ and $B\|c$ ($B = 0.1$ T) and the lower right inset enlarges the sudden drop of resistivity around 9 K. (d) The PXRD for $SmAgSb_2$ on (001) surface. The inset shows the image of a typical single crystal.

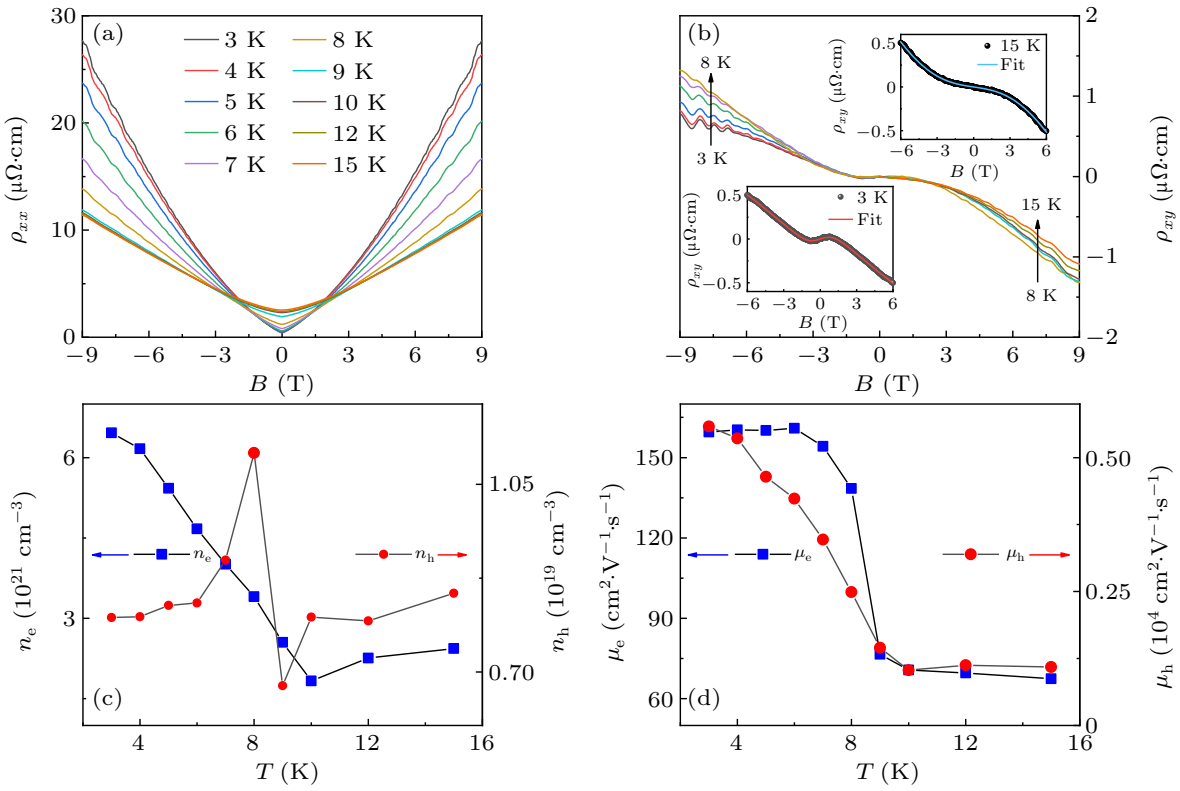


Fig. 2. (a) and (b) The longitudinal resistivities ρ_{xx} and Hall resistivities ρ_{xy} versus magnetic field for $B\|c$ within temperature range of 3 K–15 K, respectively. The insets of (b) display the fitting results of Hall resistivity by using the two-band model at 3 K and 15 K. (c) and (d) The temperature dependence of carrier densities and mobilities.

To further investigate the electronic band structure topology of $SmAgSb_2$, quantum oscillations of the ρ_{xx} and ρ_{xy} were analyzed in more details. After carefully subtracting the smooth background, denoted by $\Delta\rho_{xx}$ and $\Delta\rho_{xy}$, striking SdH oscillations at different temperatures in the range of 3 K–15 K against the reciprocal magnetic field $1/B$ are plotted in Figs. 3(a) and 3(b), which could be described by the Lifshitz–Kosevich (L–K) formula[51,52]

$$\Delta\rho \propto R_{\rm T}R_{\rm D}R_{\rm S}\cos\left[2\pi\left(\frac{F}{B}+\gamma-\delta\right)\right],$$

where $R_{\rm T} = (2\pi^2 k_{\rm B}T/(\hbar\omega_{\rm c}))/\sinh(2\pi^2 k_{\rm B}T/(\hbar\omega_{\rm c}))$, $R_{\rm D} = \exp(2\pi^2 k_{\rm B}T_{\rm D}/(\hbar\omega_{\rm c}))$, and $R_{\rm S} = \cos(\pi g m^*/(2m_{\rm e}))$ represent the damping factors caused by temperature, scattering, and spin splitting, respectively. The m^* denotes the effective cyclotron mass, $m_{\rm e}$ is the free electron mass, $k_{\rm B}$ is the Boltzmann constant, $\hbar$ is the reduced Planck's constant, F is the SdH fundamental frequency, $\omega_{\rm c} = eB/m^*$ is the cyclotron frequency, $T_{\rm D}$ is the Dingle temperature and δ is the phase shift determined by the dimensionality. For 2D case, $\delta = 0$, while for the 3D case, $\delta = \pm 1/8$. The fast Fourier transform (FFT) spectra of the SdH oscillations, depicted in Figs. 3(c) and 3(d), expose two fundamental frequencies at $\alpha = 78.6$ T and $\beta = 59.0$ T. Another frequency $\alpha^* = 0.5\alpha$ appears in FFT spectra of $\Delta\rho_{xx}$ but not in that of $\Delta\rho_{xy}$. Actually, α^* and α are the harmonic values and originate from the same Fermi surface (FS). The fundamental frequency α is present when the temperature is below 8 K; however, it disappears and β emerges when the temperature is increased. The corresponding external cross-sectional areas of the FS are $A = 0.75$ nm^{-2} and 0.56 nm^{-2}, respectively, calculated by using the Onsager relation $F = (\hbar/(2\pi e))A_{\rm F}$. The effective cyclotron mass m^* at $E_{\rm F}$ was obtained by fitting the temperature dependent FFT amplitude by the temperature damping factor $R_{\rm T}$, as shown in Fig. 3(e). The fitted m^* from the FFT amplitude of $\Delta\rho_{xx}$ and $\Delta\rho_{xy}$ are $0.211m_{\rm e}$ and $0.260m_{\rm e}$ for α. The values are very close, suggesting the reliability of the fitting. The Fermi wave vector $k_{\rm F}$ is estimated as 0.488 nm^{-1} through $k_{\rm F} = (2eF/\hbar)^{1/2}$ and the large Fermi velocity $v_{\rm F} = 2.68\times10^5$ ms^{-1} is calculated from $v_{\rm F} = \hbar k_{\rm F}/m^*$. Given that there are only four temperature data points for the frequency β, a discussion of its parameters makes no sense. The results are summarized in Table 1.

Table 1. Parameters derived from the SdH oscillations of $SmAgSb_2$.

	F (T)	A (nm^{-2})	$k_{\rm F}$ (nm^{-1})	$v_{\rm F}$ (m/s)	$m^*/m_{\rm e}$	$\varphi_{\rm B}$
α	78.6	0.75	0.488	268224	0.211	-0.166π
β	59.0	0.56	0.423	–	–	0.958π
γ	204.0	1.94	0.787	196926	0.463	0.168π
δ	528.4	5.04	1.266	243351	0.603	0.244π
θ	622.4	5.93	1.374	246913	0.645	1.154π
ϕ	1277.9	12.18	1.969	271023	0.842	-0.084π

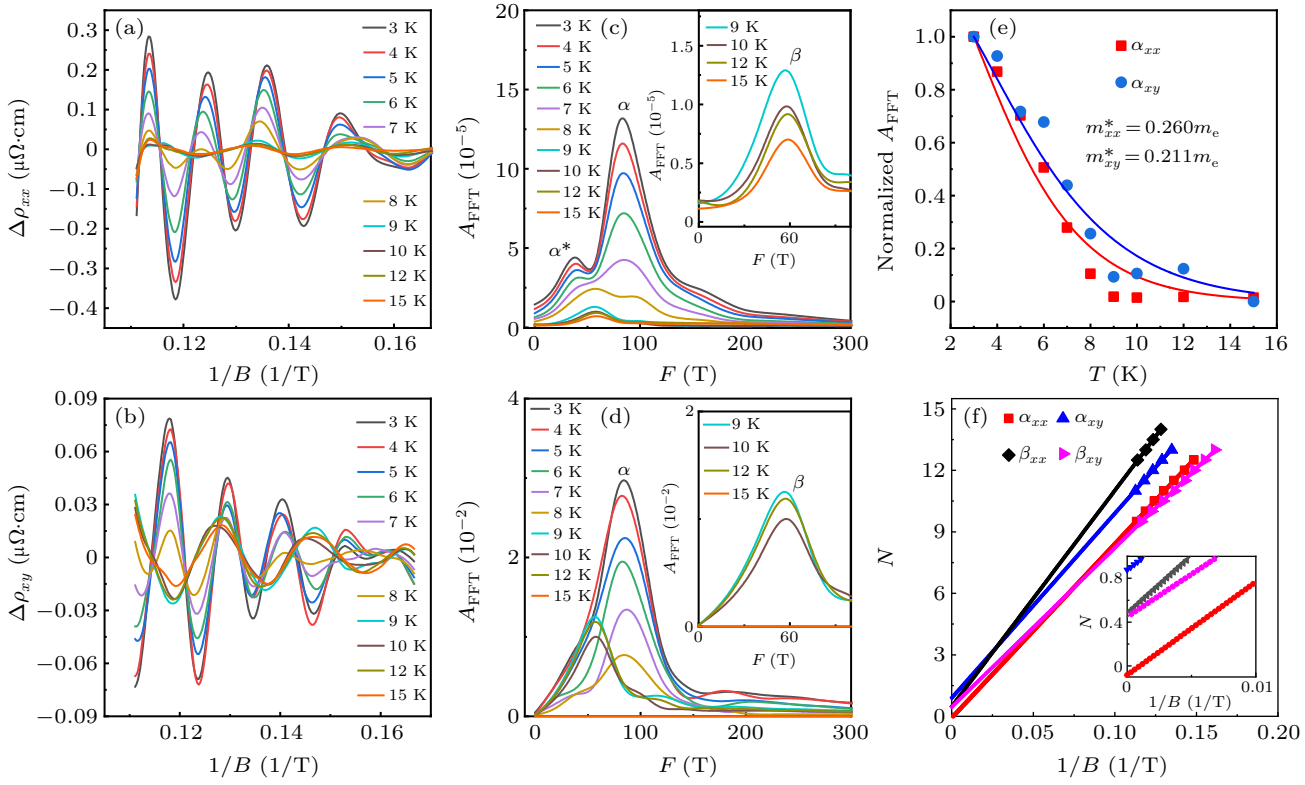


Fig. 3. (a) and (b) Quantum oscillations for longitudinal and Hall resistivities vs. $1/B$ respectively obtained by subtracting a smooth background at various temperatures. (c) and (d) The FFT spectra of $\Delta\rho_{xx}$ and $\Delta\rho_{xy}$. The insets show the frequency of β at 9 K–15 K. (e) Temperature dependence of relative amplitudes of the FFT spectra for the frequency of α from (c) and (d). The solid line is the fitting result by using L–K formula. (f) Landau fan diagram for the frequencies of α and β. Inset shows the intercepts for the linear fitting.

The topological system can generate a nontrivial Berry phase φ_B under an applied magnetic field, which can be probed by using either the Landau level (LL) index fan diagram or a direct fit to the SdH oscillations by employing the L–K formula. The phase factor γ is expressed as $1/2-\varphi_B/(2\pi)$, in which φ_B is the Berry phase. Figure 3(f) shows the plot of LL index N as a function of $1/B$ for the fundamental frequencies α and β. Here the valley positions for $\Delta\rho_{xx}$ and $\Delta\rho_{xy}$ were assigned to be integer indices (n) and the peak positions were assigned to be half-integer indices ($n-1/2$). All the points almost fall on a straight line, thus allowing a linear fit and giving the intercepts of α_{xx} and α_{xy} being ~ -0.083 and ~ 0.877, which could give nearly zero Berry phase and therefore, the fundamental frequency α is in fact trivial. However, the intercepts of β_{xx} and β_{xy} are ~ 0.479 and ~ 0.449, respectively, demonstrating a π Berry phase and nontrivial band structure topology. It should be noted that as the temperature decreases, the nontrivial β transforms into the trivial α, indicating a topological phase transition caused by the AFM order.

Figure 4(a) shows the magnetoresistance (MR), defined as $[\rho(B)-\rho(0)]/\rho(0)\times 100\%$ where $\rho(B)$ and $\rho(0)$ represent the resistivity with and without B, at a temperature range of 2 K–10 K with magnetic field up to 29 T. It reaches $\sim 6.2\times 10^3\%$ at 2 K and 26 T. The SdH oscillations are much clearer when $B>16$ T and the subtracted quantum oscillations versus $1/B$ are plotted in Fig. 4(b). The FFT results show four dominant frequencies $\gamma=204.0$ T, $\delta=528.4$ T, $\theta=622.4$ T and $\phi=1277.9$ T as presented in Fig. 4(c). The corresponding effective masses and Landau levels are fitted in Figs. 4(d) and 4(e), respectively. The results unveil the Berry phases of 0.168π, 0.244π, 1.154π and -0.084π for γ, δ, θ and ϕ, respectively. The Berry phase of θ is near π, indicating the nontrivial band structures under strong magnetic field, which while was not probed under the low magnetic field, suggesting that the large magnetic field strongly influences the FS of $SmAgSb_2$.

The nontrivial topological band structure can also be investigated by measuring the dHvA quantum oscillations. The dHvA oscillations can be nicely fitted by L–K formula[53]

$$\Delta M \propto -B^{\lambda} R_T R_D R_S \sin\left[2\pi\left(\frac{F}{B}+\gamma-\delta\right)\right],$$

where the exponent λ is determined by the dimensionality of the material, that is, $\lambda=1/2$ and 0 for the 3D and 2D cases, respectively. The magnetic field dependent isothermal magnetizations $M(B)$ of $SmAgSb_2$ up to 7 T with $B\|c$-axis at various temperatures are shown in Fig. 5(a), which exhibits striking quantum oscillations at low temperatures with the oscillation magnitude even reaching approximately 1.35×10^2 emu/mol at 10 K. After carefully subtracting the smooth background, remarkable periodic oscillations are visible in ΔM even up to 30 K as shown in Fig. 5(b).

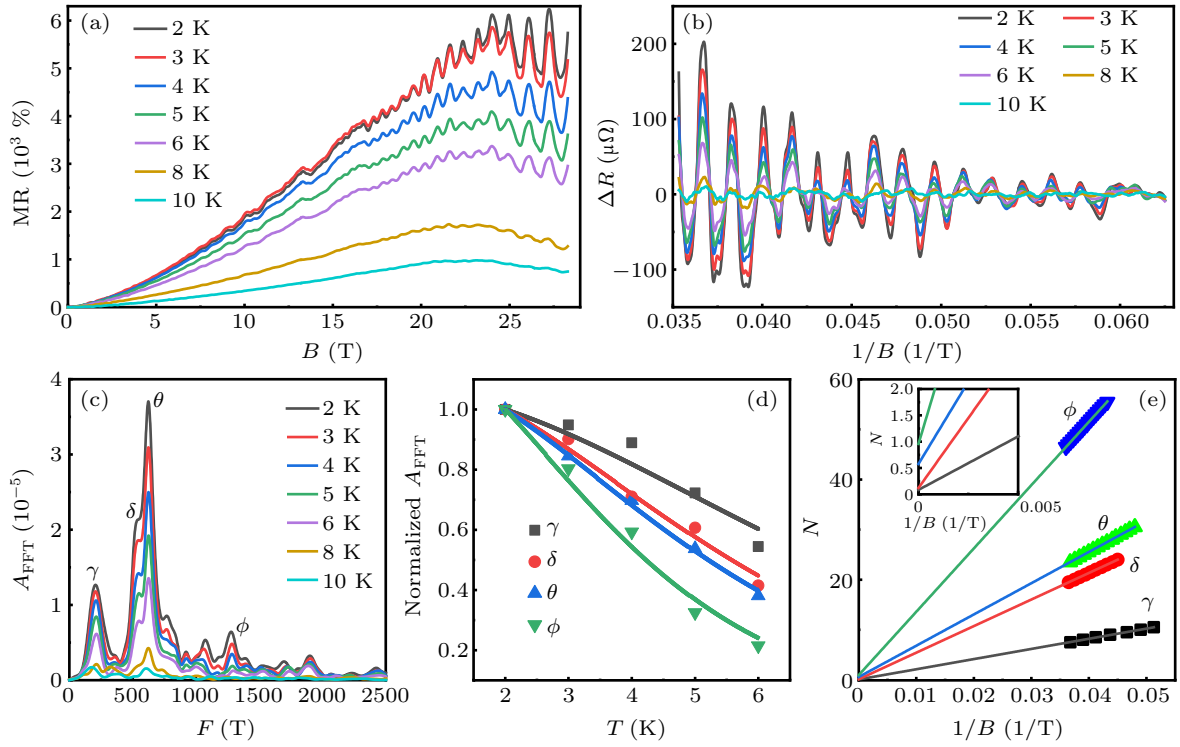


Fig. 4. (a) The MR at 2 K–10 K with magnetic field up to 29 T. (b) Quantum oscillations for longitudinal resistance vs. $1/B$ obtained by subtracting a smooth background at various temperatures. (c) The FFT spectra of ΔR and four fundamental frequencies are labeled as γ, δ, θ and ϕ, respectively. (d) Temperature dependence of relative amplitudes of the FFT spectra for four fundamental frequencies. (e) Landau fan diagram for the four frequencies and the intercepts for them are enlarged in the inset.

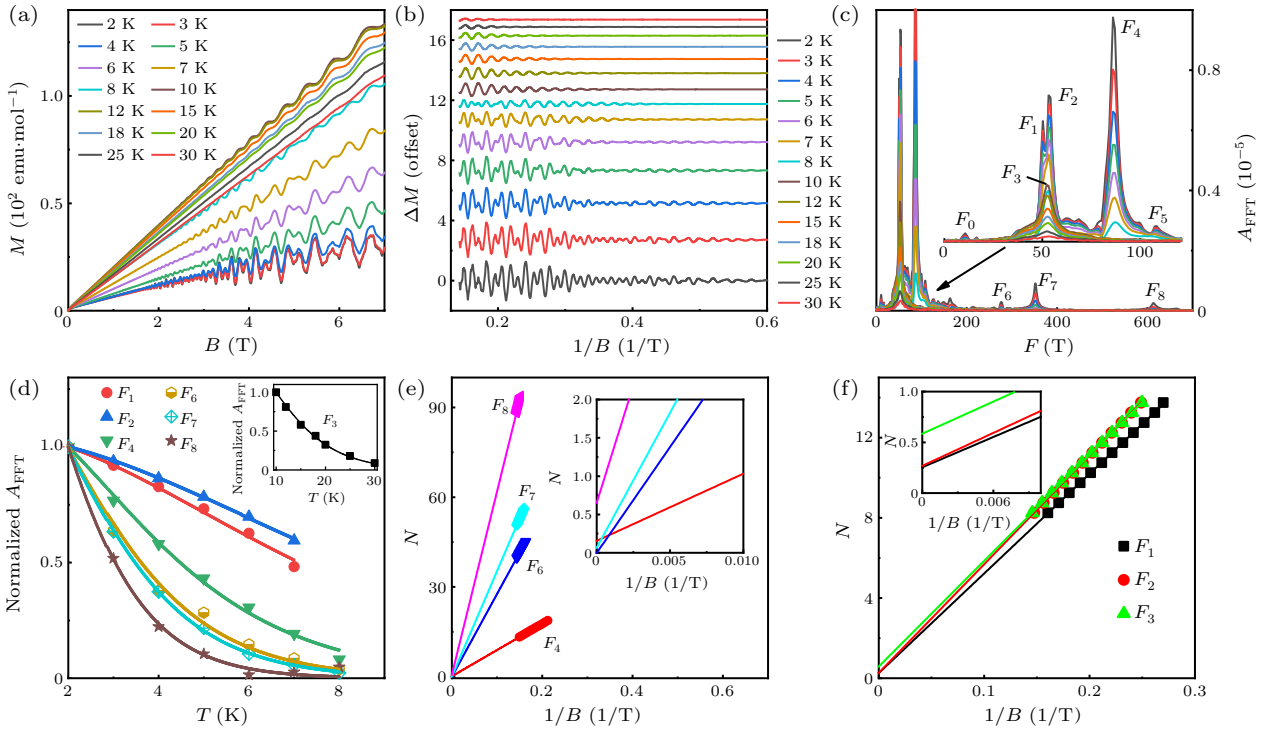


Fig. 5. (a) Magnetizations and (b) the quantum oscillations of $SmAgSb_2$ for $B\|c$ at various temperatures. (c) FFT spectra of ΔM at various temperatures. (d) Temperature dependence of relative FFT amplitudes of the oscillations. (e) and (f) Landau indexes N against $1/B$ at 2 K. Insets enlarge the fitting intercepts.

The FFT spectra of the dHvA oscillations are depicted in Fig. 5(c), in which the exposed nine fundamental frequencies are labeled as F_0 to F_8. It is clear that $F_2 = 5F_0$ and $F_5 = 2F_2$, suggesting they are originated from the same FS. Since F_0 and F_5 are relatively small, they will not be discussed herein. F_1 and F_2 are very close and they disappear and merge into F_3 as the temperature is increased above 8 K, indicating that they are sensitive to the AFM order. By fitting the thermal factor R_T, the effective cyclotron masses m^* of these frequencies at E_F are estimated and shown in Fig. 5(d). With the obtained parameters of effective masses and oscillation frequencies, we further calculated A, v_F and k_F, which are summarized in Table 2. The LL index fan diagrams for the frequencies F_1 to F_8 are constructed to examine the Berry phase. Different from the SdH oscillations, the Landau indices at the peak and valley positions of ΔM should be decreased by $1/4$. This adjustment is due to the difference between the cosine function and the sine function in the L–K formulas. Hence, we assigned Landau indices to be $n - 1/2 - 1/4$ at peak positions and $n - 1/4$ at valley positions. The LL index fan diagram is depicted in Fig. 5(e). Due to the close relationship among the fundamental frequencies F_1, F_2 and F_3, the LL fan diagram for them is plotted in Fig. 5(f), in which the intercepts give the Berry phases of 0.508π, 0.536π and 1.170π for F_1, F_2 and F_3, respectively. Apparently, the PM state hosts a nontrivial Berry phase, which becomes trivial in the AFM state. This behavior is consistent with the observed changes in α and β obtained from the SdH quantum oscillations. The information of F_1 to F_8 is summarized in Table 2.

Table 2. Parameters derived from the dHvA oscillations of $SmAgSb_2$.

	F (T)	A (nm^{-2})	k_F (nm^{-1})	v_F (m/s)	m^*/m_e	φ_B
F_1	50.3	0.48	0.391	1371954	0.033	0.508π
F_2	53.6	0.51	0.403	1669144	0.028	0.536π
F_3	52.6	0.50	0.400	2723412	0.017	1.170π
F_4	86.4	0.82	0.512	1023053	0.058	0.312π
F_6	276.6	2.64	0.916	1327106	0.080	-0.004π
F_7	352.5	3.36	1.034	1410035	0.085	0.132π
F_8	614.5	5.86	1.366	1425632	0.111	1.306π

Since the magnetic structure in the AFM state has not been experimentally determined, we calculated the energy of ferromagnetic (FM), A-type and C-type AFM magnetic structures. As shown in Fig. 6, the results suggest that A-type AFM magnetic configuration has the lowest energy, consistent with the previous study.[45] The electronic band structures of $SmAgSb_2$ in both PM and AFM states with the spin–orbit coupling (SOC) were calculated, as presented in Figs. 7(a) and 7(b), respectively. The E_F crosses both the valence and conduction bands, suggesting our above analysis of magneto-transport via adopting the two-band model is reasonable. The calculation results indicate that the topology in $SmAgSb_2$ can be described by Z_2 invariants. In PM state, the system has nonzero Z_2 of (1;000), indicating that it is a nontrivial topological insulator (TI). However, it is trivial in the AFM ground state with $Z_2 = (0;000)$. The orbitals resolved band struc-

tures in PM state, as shown in Figs. 7(c) and 7(d), show the nontrivial electronic structures. In Fig. 7(c), the existence of SOC leads to the band inversion between Ag-d and Sb_1-p_{xy} as marked by the blue frame along M–Γ path. On the other hand, the Dirac point (DP) at X below E_F is observed in Fig. 7(d) of Sb_2-p_{xy} orbital, of which the Sb_2 atoms form the square net. In the AFM state, the DP disappears and the band inversion is shifted away from E_F, thus resulting in the trivial band structures. Hence, a topological phase transition is revealed, consistent with the results of SdH and dHvA quantum oscillations which show nontrivial frequencies β (SdH) and F_3 (dHvA) in the PM state and trivial frequencies α (SdH), F_1 and F_2 (dHvA) in the AFM state.

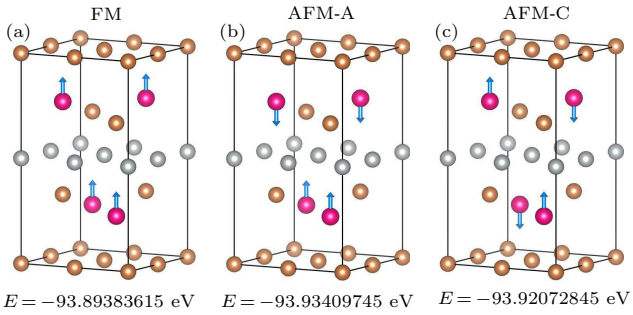


Fig. 6. The schematic (a) FM, (b) A-type and (c) C-type AFM structures of $SmAgSb_2$ in the doubled magnetic unit cell. The arrows on Sm^{3+} represent the spin directions, which are parallel or antiparallel to the c axis.

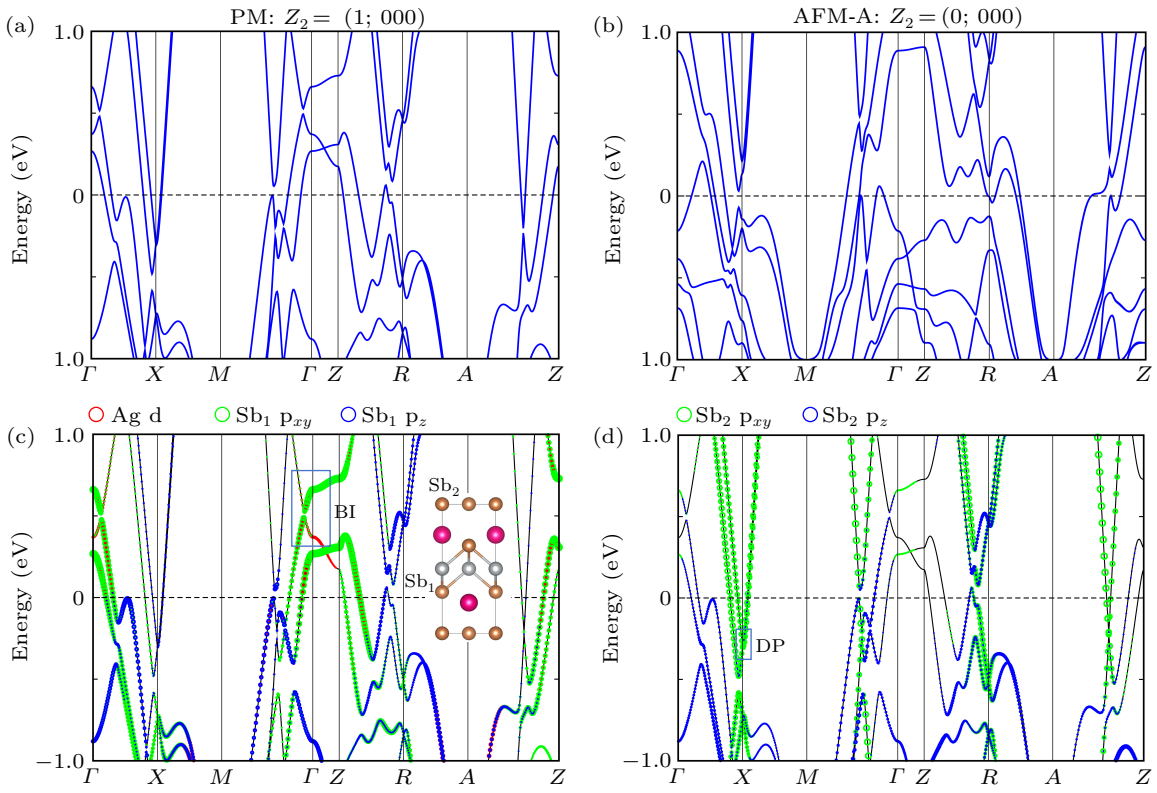


Fig. 7. The electronic structures for (a) PM and (b) A-type AFM states of $SmAgSb_2$ with considering the SOC. (c) and (d) Orbitals resolved bulk band structures of $SmAgSb_2$ in the PM state. Inset of (c) labels the Sb_1 and Sb_2 atoms. Blue frames in (c) and (d) show the band inversion (BI) and Dirac point.

4. Conclusion

Our magnetotransport and magnetization measurements on $SmAgSb_2$ crystals unveil high carrier mobility, large magnetoresistance and striking quantum oscillations. The careful analysis of the SdH and dHvA quantum oscillations uncovers nontrivial topological state in the paramagnetic phase and trivial state in the antiferromagnetic phase. Furthermore, our experimental measurements and theoretical analysis reveal a magnetism-induced topological phase transition. Additionally, there is a nontrivial Berry phase revealed by SdH oscillations under immense field. The results not only shed light onto the complex correlation between magnetism and topological properties, but also provide a new topological material with the nontrivial topological states generated by the 2D Sb square nets.

Acknowledgments

Project supported by the National Natural Science Foundation of China (Grant Nos. 12004405, 12334008, and 12374148), the Double First-Class Initiative Fund of ShanghaiTech University, and the Analytical Instrumentation Center of ShanghaiTech University (Grant No. SPST-AIC10112914). W. Xia acknowledges the research fund from the Shanghai Sailing Program (Grant No. 23YF1426900). R. D. Zhong ac-

knowledges the fund from the National Key R&D Program of China (Grant Nos. 2022YFA1402702 and 2021YFA1401600).

References

[1] Castro Neto A H, Guinea F, Peres N M R, Novoselov K S and Geim A K 2009 *Rev. Mod. Phys.* **81** 109
[2] Hasan M Z and Kane C L 2010 *Rev. Mod. Phys.* **82** 3045
[3] Bansil A, Lin H and Das T 2016 *Rev. Mod. Phys.* **88** 021004
[4] Zhang Y B, Tan Y W, Stormer H L and Kim P 2005 *Nature* **438** 201
[5] Novoselov K S, Jiang Z, Zhang Y, Morozov S, Stormer H, Zeitler U, Maan J C, Boebinger G S, Kim P and Geim A K 2007 *Science* **315** 1379
[6] Liang T, Gibson Q, Ali M N, Liu M, Cava R J and Ong N P 2015 *Nat. Mater.* **14** 280
[7] Xiong J, Kushwaha S K, Liang T, Krizan J W, Hirschberger M, Wang W D, Cava R J and Ong N P 2015 *Science* **350** 413
[8] Lv B Q, Weng H M, Fu B B, Wang X P, Miao H, Ma J, Richard P, Huang X C, Zhao L X, Chen G F, Fang Z, Dai X, Qian T and Ding H 2014 *Phys. Rev. X* **5** 031013
[9] Huang X, Zhao L, Long Y, Wang P, Chen D, Yang Z, Liang H, Xue M, Weng H, Fang Z, Dai X and Chen G 2015 *Phys. Rev. X* **5** 031023
[10] Zhang C L, Xu S Y, Belopolski I, Yuan Z J, Lin Z Q, Tong B B, Bian G, Alidoust N, Lee C C, Huang S M, Chang T R, Chang G Q, Hsu C H, Jeng H T, Neupane M, Sanchez D S, Zheng H, Wang J F, Lin H, Zhang C, Lu H. Z, Shen S Q, Neupert T, Hasan M Z and Jia S 2016 *Nat. Commun.* **7** 10735
[11] Liu E, Sun Y, Kumar N, Muechler L, Sun A, Jiao L, Yang S Y, Liu D, Liang A, Xu Q N, Kroder J, Süß V, Borrmann H, Shekhar C, Wang Z S, Xi C Y, Wang W H, Schnelle W, Wirth S, Chen Y L, Goennenwein S T B and Felser C 2018 *Nat. Phys.* **14** 1125
[12] Hsieh D, Qian D, Wray L, Xia Y, Hor Y S, Cava R J and Hasan M Z 2008 *Nature* **452** 970
[13] Zhang W, Yu R, Zhang H J, Dai X and Fang Z 2010 *New J. Phys.* **12** 065013
[14] Hsieh D, Xia Y, Qian D, Wray L, Dil J H, Meier F, Osterwalder J, Patthey L, Checkelsky J G, Ong N P, Fedorov A V, Lin H, Bansil A, Grauer D, Hor Y S, Cava R J and Hasan M Z 2009 *Nature* **460** 1101
[15] Chen Y L, Chu J H, Analytis J G, Liu Z K, Igarashi K, Kuo H H, Qi X L, Mo S K, Moore R G, Lu D H, Hashimoto M, Sasagawa T, Zhang S C, Fisher I R, Hussain Z and Shen Z X 2010 *Science* **329** 659
[16] Li J H, Li Y, Du S Q, Wang Z, Gu B L, Zhang S C, He K, Duan W H and Xu Y 2019 *Sci. Adv.* **5** aaw5685
[17] Zhang D Q, Shi M J, Zhu T S, Xing D Y, Zhang H J and Wang J 2019 *Phys. Rev. Lett.* **122** 206401
[18] Teng X K, Chen L B, Ye F, Rosenberg E, Liu Z Y, Yin J X, Jiang Y X, Oh J S, Hasan M Z, Neubauer K J, Gao B, Xie Y F, Hashimoto M, Lu D H, Jozwiak C, Bostwick A, Rotenberg E, Birgeneau R J, Chu J H, Yi M and Dai P C 2022 *Nature* **609** 490
[19] Farhan M A, Lee G and Shim J H 2014 *J. Phys.: Condens. Matter* **26** 042201
[20] Sakai H, Fujimura H, Sakuragi S, Ochi M, Kurihara R, Miyake A, Tokunaga M, Kojima T, Hashizume D, Muro T, Kuroda K, Kondo K, Kida T, Hagiwara M, Kuroki K, Kondo M, Tsuruda K, Murakawa H and Hanasaki N 2020 *Phys. Rev. B* **101** 081104
[21] Liu B, Yu F, Cheng J B, Zhu W L, He J B, Liu C B, Li L and Luo Y S 2022 *J. Supercond. Nov. Magn.* **35** 3263
[22] You J S, Lee I, Choi E S, Jo Y J, Shim J H and Kim J S 2019 *Current Applied Physics* **19** 230
[23] Park J, Lee G, Wolff-Fabris F, Koh Y Y, Eom M J, Kim Y K, Farhan M A, Jo Y J, Kim J H, Shim J H and Kim J S 2011 *Phys. Rev. Lett.* **107** 126402
[24] Zhang A M, Liu C L, Yi C J, Zhao G H, Xia T L, Ji J T, Shi Y G, Yu R, Wang X Q, Chen G F and Zhang Q M 2016 *Nat. Commun.* **7** 13833
[25] Li L J, Wang K F, Graf D, Wang L M, Wang A F and Petrovic C 2016 *Phys. Rev. B* **93** 115141
[26] Masuda H, Sakai H, Tokunaga M, Yamasaki Y, Miyake A, Shiogai J, Nakamura S, Awaji S, Tsukazaki A, NaKao H, Murakami Y, Arima T H, Tokura Y and Ishiwata S 2016 *Sci. Adv.* **2** 1501117
[27] Sun Z L, Wang A F, Mu H M, Wang H H, Wang Z F, Wu T, Wang Z Y, Zhou X Y and Chen X H 2021 *npj Quantum Mater.* **6** 94
[28] Wang K F, Graf D, Wang L M, Lei H C, Tozer S W and Petrovic C 2012 *Phys. Rev. B* **85** 041101
[29] Soh J R, Manuel P, Schröter N M B, Yi C J, Shi Y G, Prabhakaran D and Boothroyd A T 2019 *Phys. Rev. B* **100** 174406
[30] Borisenko S, Evtushinsky D, Gibson Q, Yaresko A, Koepernik K, Kim T, Ali M, Brink J V D, Hoesch M, Fedorov A, Haubold E, Kushnirenko Y, Soldatov I, Schäfer R and Cava R J 2019 *Nat. Commun.* **10** 3424
[31] Pan Y, Le C, He B, Watzman S J, Yao M Y, Gooth J, Heremans J P, Sun Y and Felser C 2022 *Nat. Mater.* **21** 203
[32] Shiomi Y, Watanabe H, Masuda H, Takahashi H, Yanase Y and Ishiwata S 2019 *Phys. Rev. Lett.* **122** 127207
[33] Shi X, Richard P, Wan K F, Liu M, Matt C E, Xu N, Dhaka R S, Ristic Z, Qian T, Yang Y F, Petrovic C, Shi M and Ding H 2016 *Phys. Rev. B* **93** 081105
[34] Sawani D, Khadiza A, Rahul V, Bahadur S, Saroj P D, Thamizhavel A and Maiti K 2023 arXiv:2311.05278 [cond-mat.str-el]
[35] Blöchl P E 1994 *Phys. Rev. B* **50** 17953
[36] Lehtomäki J, Makkonen I, Caro M A, Harju A and Lopez-Acevedo O 2014 *J. Chem. Phys.* **141** 234102
[37] Perdew J P, Burke K and Ernzerhof M 1996 *Phys. Rev. Lett.* **77** 3865
[38] Perdew J P and Wang Y 1992 *Phys. Rev. B* **45** 13244
[39] Kresse G and Hafner J 1993 *Phys. Rev. B* **47** 558
[40] Kresse G and Furthmüller J 1996 *Comput. Mater. Sci.* **6** 15
[41] Kresse G and Furthmüller J 1996 *Phys. Rev. B* **54** 11169
[42] Vladimir I A, Aryasetiawan F and Lichtenstein A I 1997 *J. Phys. Condens. Matter* **9** 767
[43] Marzari N and Vanderbilt D 1997 *Phys. Rev. B* **56** 12847
[44] Wu Q S, Zhang S N, Song H F, Troyer M and Soluyanov A A 2018 *Comput. Phys. Commun.* **224** 405
[45] Prozorov R, Vannette M D, Samolyuk G D, Law S A, Bud'ko S L and Canfield P C 2007 *Phys. Rev. B* **75** 014413
[46] Myers M D, Bud'ko S L, Antropov V P, Harmon B N, Canfield P C and Lacerda A H 1999 *Phys. Rev. B* **60** 13371
[47] Myers M D, Bud'ko S L, Fisher I R, Islam Z, Kleinke H, Lacerda A H and Canfield P C 1999 *J. Magn. Magn. Mater.* **205** 27
[48] Rourke P M C, Bangura A F, Proust C, Levallois J, Leyraud N D, LeBoeuf D, Taillefer L, Adachi S, Sutherland M L and Hussey N E 2010 *Phys. Rev. B* **82** 020514
[49] Ishiwata S, Shiomi Y, Lee J S, Bahramy M S, Suzuki T, Uchida M, Arita R, Taguchi Y and Tokura Y 2013 *Nat. Mater.* **12** 512
[50] Li C Z, Li J G, Wang L X, Zhang L, Zhang J M, Yu D P and Liao Z M 2016 *ACS Nano* **10** 6020
[51] Luk'yanchuk I A and Kopelevich Y 2006 *Phys. Rev. Lett.* **97** 256801
[52] He L P, Hong X C, Dong J K, Pan J, Zhang Z, Zhang J and Li S Y 2014 *Phys. Rev. Lett.* **113** 246402
[53] Mikitik G P and Sharlai Y V 1999 *Phys. Rev. Lett.* **82** 2147